

Kinematical signatures of hidden stellar discs

John Magorrian

Canadian Institute for Theoretical Astrophysics, University of Toronto, 60 St George Street, Toronto, Ontario, Canada M5S 3H8

ABSTRACT

The deprojection of the surface brightness distribution of an axisymmetric galaxy does not have a unique solution unless the galaxy is viewed precisely edge-on. I present an algorithm that finds the full range of smooth axisymmetric density distributions consistent with a given surface brightness distribution and inclination angle, and use it to investigate the effects of this non-uniqueness on the line-of-sight velocity profiles (VPs) of two-integral models of both real and toy discy galaxies viewed at a range of inclination angles. Photometrically invisible face-on discs leave very clear signatures in the minor-axis VPs of the models (Gauss–Hermite coefficients $h_4 \gtrsim 0.1$), provided the disc-to-bulge ratio is greater than about 3%. I discuss the implications of these hitherto neglected discs for dynamical modelling.

Key words: celestial mechanics, stellar dynamics – galaxies: elliptical and lenticular – galaxies: kinematics and dynamics – galaxies: structure

1 INTRODUCTION

A fundamental problem in astronomy is determining the distribution of intrinsic shapes of elliptical galaxies. One way to do this is by assuming that every galaxy is a triaxial ellipsoid, and then to use simple photometrical and kinematical information to try to constrain the distribution of axis ratios of their outer regions (e.g., Binney 1985; Franx, Illingworth & de Zeeuw 1991; Statler 1994). About a third of all ellipticals, however, have “discy” isophote distortions (Bender et al. 1989), steep power-law central density cusps, and show no obvious indications of triaxiality (Faber et al. 1997; Kormendy & Bender 1996; see also Merritt & Quinlan 1998). Little is known about the discs that most probably cause these distortions. For example, it is unclear whether discy ellipticals form a continuous sequence in disc-to-bulge ratio with S0 galaxies (Scorza & Bender 1995). Moreover, it is possible that quite large discs could lurk in those power-law galaxies that do not have obvious isophote distortions: Rix & White (1990) have shown that even the large discs in S0 galaxies are photometrically undetectable for about 50% of orientation angles. Therefore, rather than trying to determine axis ratios for these power-law galaxies under the assumption of ellipsoidal symmetry, it is perhaps more interesting to use kinematical information to try to determine (or at least constrain) their full central stellar density distributions $\rho(R, z)$ under the assumption of axisymmetry.

The ease with which discs can be hidden can be understood using the Fourier slice theorem (Rybicki 1987): in Fourier space, the surface brightness distribution of an axisymmetric galaxy with a given inclination angle i provides information about the density only outside a “cone of ignorance” of opening angle $90^\circ - i$ around the galaxy’s symmetry axis, where $i = 90^\circ$ for an edge-on galaxy. Gerhard & Binney (1996) have explicitly constructed a family of disc-like “konus densities” whose Fourier transforms vanish

outside the cone of ignorance, and therefore whose densities project to zero surface brightness. Thus, the photometric deprojection problem is not unique for non-edge-on galaxies: any solution $\rho(R, z)$ is degenerate to the addition of disc-like konus densities. Further examples of konus densities are given by Kochanek & Rybicki (1996) and van den Bosch (1997).

Konus densities are quite difficult to construct analytically, so a numerical approach is needed to explore the full range of possible solutions to the photometric deprojection problem. Such an approach was taken by Romanowsky & Kochanek (1997; hereafter RK) who used a maximum penalized likelihood algorithm, penalizing their solutions with “bias functions” that influenced the shape of the final solution chosen, as well as providing the smoothness criterion that is necessary for any discrete numerical approximation. They found that the uncertainties in the deprojection were even greater than one would expect from the simple analytical examples of konus densities above. RK also used Jeans equations modelling to predict the projected second-order velocity moments corresponding to each solution, under the assumption of a constant mass-to-light ratio and a two-integral distribution function. They found that the second-order moments were only very weakly affected by the non-uniqueness of the deprojection: different solutions gave almost identical projected second-moment profiles.

Real kinematical measurements, however, include more information than just the second-order velocity moments. Indeed, nowadays one routinely measures the full line-of-sight velocity profiles (VPs) of galaxies. In this paper, I use simple models to investigate whether using VPs can place stronger constraints on the intrinsic shapes of axisymmetric galaxies. It is organized as follows. Section 2 describes the deprojection problem in numerical terms and gives my method of solution. Like RK, I use maximum penalized likelihood, but with a penalty function that trades off the ele-

gance of their bias functions for comprehensibility and ease of use. I also use an interpolation scheme that is better able to handle the cusped density profiles present in real galaxies. In Section 3, I demonstrate the effects that konus densities have on the VPs of simple toy galaxy models. The discs in real galaxies are not strict konus densities, so in Section 4 I use models of some real edge-on discy ellipticals to investigate whether their VPs would contain any signature of the discs were they viewed closer to face on. Section 5 sums up and suggests future work.

2 NUMERICAL SOLUTION OF THE PHOTOMETRIC DEPROJECTION PROBLEM

For projected quantities, let us choose a system of coordinates (x', y', z') with origin O at the centre of the galaxy, the Oz' -axis parallel to the line of sight to the galaxy, and the Ox' -axis parallel to the galaxy's projected major (minor) axis for an oblate (prolate) model. Real galaxies are close to spheroidal, so assume that we are given discrete measurements of the projected surface brightness distribution $I(x', y')$ on an elliptical polar grid (m', θ') with $n_{m'} \times n_{\theta'}$ vertices at

$$\begin{aligned} x'_{ij} &= m'_i \cos \theta'_j \\ y'_{ij} &= q' m'_i \sin \theta'_j, \end{aligned} \quad (1)$$

where m'_i runs logarithmically between the radii of the inner- and outer-most isophotes, θ'_j is spaced linearly between 0 and $\pi/2$, and q' ($1/q'$) is the mean projected axis ratio of the galaxy assuming it is oblate (prolate). Let $\mathcal{S}_{ij} \equiv \log I(m'_i, \theta'_j)$ and let $\Delta \mathcal{S}_{ij}$ be the corresponding measurement error (assumed Gaussian).

We seek a three-dimensional luminosity density $\rho(R, z)$, which, when viewed at a given inclination angle i , projects to an acceptable fit to this \mathcal{S}_{ij} . We expect this $\rho(R, z)$ to be roughly spheroidal, and to have a radial profile that is locally well-approximated by some power law. Hence I represent $\rho(R, z)$ as $\mathcal{R}(m, \theta) \equiv \log \rho(m, \theta)$ on an $n_m \times n_\theta$ grid with vertices at

$$\begin{aligned} R_{ij} &= m_i \cos \theta_j \\ z_{ij} &= q m_i \sin \theta_j, \end{aligned} \quad (2)$$

where the intrinsic axis ratio q is related to q' by $q'^2 = q^2 \sin^2 i + \cos^2 i$, θ_j runs linearly from 0 to $\pi/2$, and m_i runs logarithmically from m'_1 to a few times m'_{n_m} . Values of $\rho(m, \theta)$ between grid points are obtained by interpolating linearly in \mathcal{R} and exponentiating. The calculation of the model's projected surface brightness $\hat{\mathcal{S}}_{ij}$ on the grid (1) is outlined in the Appendix.

Given these $\hat{\mathcal{S}}_{ij}$, the goodness of fit is measured by

$$\chi^2 = \sum_{i=1}^{n_{m'}} \sum_{j=1}^{n_{\theta'}} \left(\frac{\mathcal{S}_{ij} - \hat{\mathcal{S}}_{ij}}{\Delta \mathcal{S}_{ij}} \right)^2. \quad (3)$$

A reasonable model will have $\chi^2 \simeq n_{m'} n_{\theta'} \pm \sqrt{2 n_{m'} n_{\theta'}}$.

There will be many distributions \mathcal{R}_{ij} that will have a value of χ^2 in this range, but not all of them will be acceptably smooth. In addition, one would like the ability to choose among the various acceptable solutions, for example by preferring those with a given degree of disciness or boxiness. Given these reasonable prior prejudices (let us denote

them as I), and an observed \mathcal{S}_{ij} , Bayes' theorem gives the relative plausibility of any set of \mathcal{R}_{ij} as

$$p(\mathcal{R} | \mathcal{S}, I) \propto p(\mathcal{S} | \mathcal{R}, I) p(\mathcal{R} | I), \quad (4)$$

where the likelihood $p(\mathcal{S} | \mathcal{R}) = \exp(-\frac{1}{2}\chi^2)$ and the prior $p(\mathcal{R} | I)$ expresses our preconceptions (smoothness, isocontour shape) about the form of $\rho(R, z)$. Taking the logarithm of equation (4) yields an expression for the penalized log-likelihood

$$\mathcal{L} \equiv -\frac{1}{2}\chi^2 + P_I[\mathcal{R}], \quad (5)$$

where the penalty function $P_I[\mathcal{R}] \equiv \log p(\mathcal{R} | I)$ penalizes those solutions that do not fit our smoothness and isocontour-shape requirements.

2.1 The penalty function

One of the simplest ways of penalizing non-smooth solutions is by using the mean-square second derivative:

$$\begin{aligned} P_{\text{smooth}}[\mathcal{R}] &= \frac{C_m}{n_\theta} \sum_{i,j} \left(\frac{\mathcal{R}_{i+1,j} - 2\mathcal{R}_{ij} + \mathcal{R}_{i-1,j}}{\Delta \log m} \right)^2 \\ &+ \frac{C_\theta}{n_m} \sum_{i,j} \left(\frac{\mathcal{R}_{i,j+1} - 2\mathcal{R}_{ij} + \mathcal{R}_{i,j-1}}{\Delta \theta} \right)^2, \end{aligned} \quad (6)$$

where C_m and C_θ are the weights given to radial and angular smoothness and I have omitted some uninteresting constant factors. Sensible values for the weights can be estimated as follows. Consider a typical galaxy with $\rho \sim m^{-4}$ in the outer parts, rolling over to $\rho \sim m^{-1}$ in the centre. Thus $\partial \mathcal{R} / \partial \log m$ changes from -4 in the outer parts to -1 near the centre, and so the first sum in equation (6) must be at least $3^2/n_m$. Choosing $C_m = -(2n_{m'} n_{\theta'})^{1/2} n_m / \lambda_m^2$, an increase in the RMS change in $\partial \mathcal{R} / \partial \log m$ by an amount λ_m is considered as bad as an one-sigma increase in χ^2 of $(2n_{m'} n_{\theta'})^{1/2}$. I choose $\lambda_m = 3$ for all the results in this paper. Similarly, for the angular smoothing weight I choose $C_\theta = -(2n_{m'} n_{\theta'})^{1/2} n_\theta / \lambda_\theta^2$. Since not much is known about galaxies' angular profiles, it is not so clear how to choose λ_θ a priori, but experiments with real galaxies show that $\lambda_\theta \simeq 0.5$ is about right.

The shape (degree of disciness or boxiness) of $\rho(m, \theta)$ can be measured by its $\cos 4\theta$ Fourier coefficients, defined as

$$c_4(m) \equiv \int_{-\pi/2}^{\pi/2} \rho(m, \theta) \cos 4\theta \, d\theta, \quad (7)$$

similar to the various definitions often used to quantify isophote shapes (e.g., Jedrzejewski 1987; Bender & Möllenhoff 1987). At radii where the model is locally discy (boxy) c_4 will be positive (negative). The penalty function

$$P_{\text{shape}}[\mathcal{R}] = \left(\frac{n_{m'} n_{\theta'}}{n_m} \right)^{1/2} \sum_i \left(\frac{c_4(m_i) - d}{\Delta d} \right)^2, \quad (8)$$

favours solutions with $c_4 \simeq d \pm \Delta d$, provided the observations do not place strong constraints on c_4 . If on the other hand the observations constrain c_4 to lie outside the range $d \pm \Delta d$, P_{shape} biases the solution towards $c_4 = d$, with the parameter Δd controlling the strength of the bias.

A final, not-so-obvious, necessary constraint on the shape of the density isocontours is that $\partial\mathcal{R}/\partial\theta$ be non-negative at $\theta = 0$ and $\pi/2$. I use

$$P_{\text{nn}} = \frac{C_{\text{nn}}}{n_m} \sum_i (\max(0, \mathcal{R}_{i,2} - \mathcal{R}_{i,1}))^2 + \frac{C_{\text{nn}}}{n_m} \sum_i (\max(0, \mathcal{R}_{i,n_\theta} - \mathcal{R}_{i,n_\theta-1}))^2, \quad (9)$$

to penalize each radial grid point that does not satisfy these conditions by an amount $C_{\text{nn}} = -4\sqrt{n_m n_{\theta'}}$.

Taking equations (6), (8) and (9) together, the full penalty function is $P_I = P_{\text{smooth}} + P_{\text{shape}} + P_{\text{nn}}$.

2.2 Finding the best solution

The following procedure is used to find the density $\rho(m, \theta)$ that maximizes the penalized log-likelihood \mathcal{L} . There may well be more efficient schemes, but this one is easy to implement and works well. First the parameters (L, m_0, α, β) of the distribution

$$\rho(m) = \frac{L}{4\pi q B(3-\alpha, 3-\beta)} \frac{m_0^{\beta-3}}{m^\alpha (m_0 + m)^{\beta-\alpha}}, \quad (10)$$

that minimize χ^2 are found using the Levenberg–Marquardt algorithm (Press et al., 1992). The function $B(\cdot, \cdot)$ in (10) is the usual Beta function. Then the following simulated annealing scheme (Metropolis et al., 1953; Press et al. 1992) is used to improve this initial $\mathcal{R}(m, \theta)$:

- (1) Calculate $\mathcal{L}[\mathcal{R}]$ for this initial guess.
- (2) Make a change $\delta\mathcal{R}$ to \mathcal{R} . Calculate $\hat{\mathcal{S}}[\mathcal{R} + \delta\mathcal{R}]$, $P_I[\mathcal{R} + \delta\mathcal{R}]$ and thus $\mathcal{L}[\mathcal{R} + \delta\mathcal{R}]$.
- (3) If $\Delta\mathcal{L} \equiv \mathcal{L}[\mathcal{R} + \delta\mathcal{R}] - \mathcal{L}[\mathcal{R}] > 0$ accept the change $\delta\mathcal{R}$; otherwise accept it with probability $\exp(\Delta\mathcal{L}/T)$, where the “temperature” T is defined below.
- (4) Go back to step 2.

In this scheme each grid point (i, j) has an associated $\Delta\mathcal{R}_{ij}$ that governs how much \mathcal{R}_{ij} can change by in step (2). The natural initial value for all the $\Delta\mathcal{R}_{ij}$ is the RMS difference between \mathcal{S}_{ij} and the $\hat{\mathcal{S}}_{ij}$ of equation (10). In step (2), each change $\delta\mathcal{R}$ is made by choosing one grid point (i, j) at random and adding $r\Delta\mathcal{R}_{ij}$ to \mathcal{R}_{ij} , where r is a random number uniformly distributed in $(-1, 1)$. Whenever a change $\delta\mathcal{R}_{ij}$ is accepted (step 3), $\Delta\mathcal{R}_{ij}$ is increased by a small factor (say 1.2); otherwise $\Delta\mathcal{R}_{ij}$ is decreased by the same factor. This ensures that the changes the program makes are as large as possible.

Given the initial $\delta\mathcal{R}_{ij}$, a few times $n_m n_\theta$ iterations of step (2) are made, and the initial temperature T is chosen to be the mean value of $|\Delta\mathcal{L}|$. This ensures that roughly half the steps will be accepted. Every $8n_m n_\theta$ iterations the temperature is set equal to the mean change in $|\Delta\mathcal{L}|$ of all the accepted steps in the previous $8n_m n_\theta$ iterations. The program stops with this temperature is less than $\sqrt{n_m n_{\theta'}}$.

3 KINEMATICAL EFFECTS OF KONUS DENSITIES

Before investigating real galaxies, it is worthwhile pausing to look at the effects that konus densities can have on simple toy galaxies. I use a Jaffe (1983) model (equation (10))

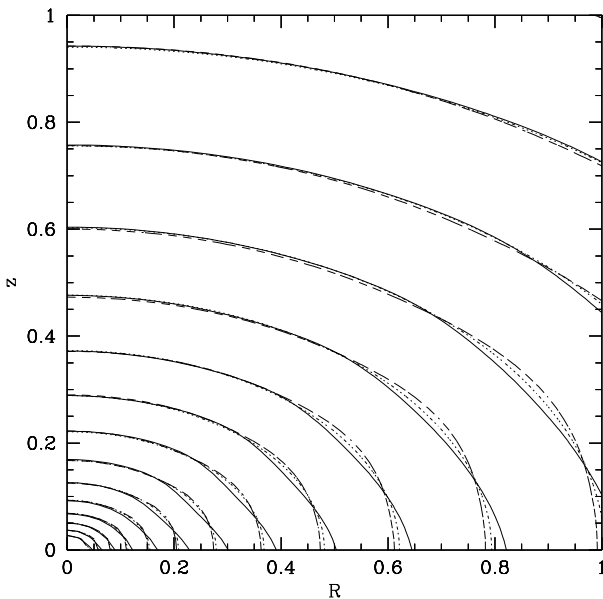


Figure 1. The most discy (solid contours) and most boxy (dashed contours) density distributions $\rho(R, z)$ that project to the surface brightness distribution of a flattened Jaffe model viewed at $i = 60^\circ$. The dotted contours plot the density of the original Jaffe model.

with $\alpha = 2$ and $\beta = 4$) with unit scale radius, unit luminosity and intrinsic axis ratio $q = 0.6$, viewed quite close to edge-on at $i = 60^\circ$. The projected surface brightness distribution is placed on the grid (1) with $n_{m'} \times n_{\theta'} = 40 \times 7$, and $m'_1 = 0.01$ and $m'_{40} = 10$. I seek the luminosity density $\rho(R, z)$ on grid (2) with $n_m \times n_\theta = 60 \times 10$ vertices with m_i running from 0.01 to 100. As a test of the accuracy of the numerical projection, placing the exact $\rho(R, z)$ on this grid and projecting yields an $\hat{\mathcal{S}}_{ij}$ that has an RMS difference of only 0.05% from the results obtained by Jaffe’s exact expression. This is much smaller than typical observational errors.

To stop the deprojection program finding the exact solution immediately, I fix $\alpha = 1.5$ in the fitting of the initial guess (equation (10)). This initial guess has $L = 0.49$, $m_0 = 0.26$, $\beta = 3.6$ and an RMS error of 0.12. With $\Delta\mathcal{S}_{ij} = 0.5\%$, $\Delta d = 0.03$, and $d = +0.1$ (discy bias) or -0.1 (boxy bias), the program stops after about 70000 iterations of the Metropolis algorithm have reduced this RMS error to around 0.56%. To look for systematic deviations between \mathcal{S}_{ij} and $\hat{\mathcal{S}}_{ij}$, I use Bender & Möllenhoff’s (1987) method to analyze the isophotes of the solutions. This yields the semi-major axis and ellipticity (a, ϵ) of the best-fit ellipse to each isophote, along with isophotal shape parameters a_4, a_6, \dots , obtained by expanding the angular dependence of the radial deviation between this best-fit ellipse and the isophote as a Fourier series. Both the boxy and discy solutions above have $a_4/a \simeq \pm 0.4\%$, which would be just on the threshold of detectability for real observations, implying that neither solution is acceptable.

Letting the program continue with $\Delta\mathcal{S}_{ij} = 0.05\%$ in each case, it stops with an RMS error of 0.03% (smaller than the 0.05% numerical accuracy) after a further 200000 or so iterations. The resulting density distributions are plotted on Fig. 1. The projection of these densities yields isophotes

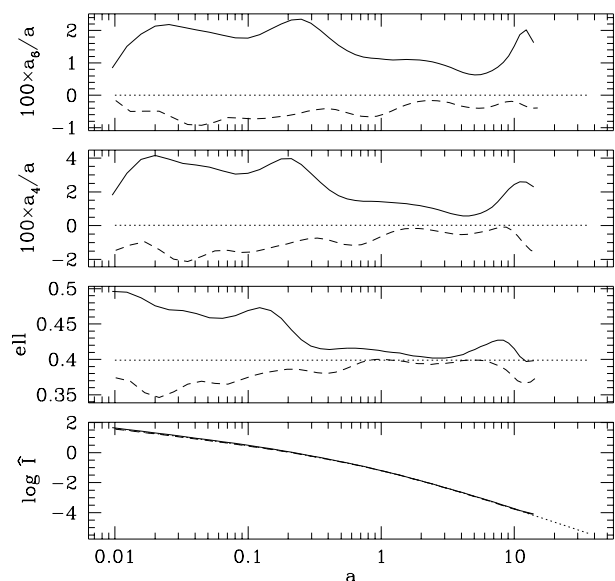


Figure 2. The surface brightness, ellipticity and isophotal shape profiles of the models in Fig. 1 viewed edge-on. I use Bender & Möllenhoff’s (1987) definition of the isophotal shape parameters a_n .

with $|a_{2n}/a| < 0.03\%$, perfectly elliptical for all practical purposes. Increasing $|d|$ and decreasing Δd does not change the solutions significantly, indicating that they are the most extreme given the smoothness constraints.

These densities project to the surface brightness profile of a Jaffe model for any $i < 60^\circ$. So, for a fraction $\cos i = 50\%$ of random orientations there is no sign of deviations from pure ellipticity in the models’ isophotes. But when the models are viewed edge-on, the disciness or boxiness becomes quite apparent (Fig. 2).

The konus density obtained by subtracting one of these solutions from the other has almost exactly the same dependence on radius as the original Jaffe model, except at the very centre where a konus density can be no steeper than r^{-1} (van den Bosch 1997). Unlike the analytical konus densities found by Gerhard & Binney (1996), Kochanek & Rybicki (1996) and van den Bosch (1997), this numerical konus density has only approximately a $\cos n\theta$ angular dependence and there are no special angles θ along which its radial profile is particularly shallow.

To investigate the kinematical effects of the photometric degeneracy, I calculate the isotropic-rotator VPs of each model using the moment-based method of Magorrian & Binney (1994). It is convenient to present the resulting VPs using the Gauss–Hermite parameterization of van der Marel & Franx (1993). This gives the parameters V and σ of the best-fitting Gaussian to each VP, along with coefficients h_3, h_4, \dots , that describe how the VP deviates from this Gaussian. VPs with prograde wings steeper than retrograde ones have $h_3 < 0$, while VPs more triangular (flat-topped) than the Gaussian have $h_4 > 0$ ($h_4 < 0$). Figure 3 shows the VPs of the discy and boxy models in this form, along with the VPs of the original Jaffe model. On the major axis the discy model has relatively high V and negative h_3 . The

slight bias towards circular orbits that causes this also affects the discy model’s minor-axis VPs, giving them significant high-velocity wings and thus raising their h_4 coefficients. (A stronger version of this phenomenon was first noted by Scorza & Bender (1995) in the minor-axis VPs of the discy elliptical NGC 4660.) The differences between the models’ Gauss–Hermite coefficients are approximately the same as the errors in high signal-to-noise measurements of real VPs. It is therefore plausible that one could use VPs to constrain the internal $\rho(R, z)$ structure of a real galaxy with a somewhat larger disc than this simple toy model.

4 KINEMATICAL EFFECTS OF REALISTIC DISCS

To investigate the detectability of discs in real galaxies, I consider what the nearby edge-on E7/S0 galaxy NGC 3115 looks like when viewed at different orientations. Scorza & Bender (1995, hereafter SB) have used a photometric disc–bulge decomposition to show that this galaxy is consistent with a razor-thin disc viewed at $i = 84^\circ$ embedded in an almost perfectly elliptical bulge. The $\rho(R, z)$ profiles I obtain by deprojecting SB’s photometry of this galaxy for $i = 84^\circ$ and $i = 90^\circ$ (Fig. 4) show that it can equally well be considered as a reasonably fat disc-like component embedded in a slightly boxy bulge-like component. Since the galaxy is viewed close to edge-on, it may be possible to distinguish between the thin- and fat-disc models using the a_8 and higher-order isophote shape coefficients and a great deal of care (or, perhaps more sensibly, by dropping the a_n parameterization altogether). In what follows, let us assume that NGC 3115 is reasonably well described by my $i = 84^\circ$ model, with a constant mass-to-light ratio and an two-integral distribution function. None of these assumptions are strictly true, but this simple model does serve to illustrate some important points.

Suppose we view the galaxy close to face-on, at $i = 30^\circ$. Fig. 5 shows that in this case the maximum value of a_4/a is only 0.2% – there is no indication of disciness in the photometry. The disc does, however, make itself evident in the model’s minor-axis VPs, since the extra circular orbits seen from above make the VPs more centrally peaked, giving them large positive values of h_4 (solid curve in top panel). For comparison, deprojecting the $i = 30^\circ$ surface brightness distribution with penalty function P_{shape} parameters $d = 0$ and $\Delta d = 4(a_4/a)_{\text{max}} = 0.8\%$ yields the model with the most closely spheroidal isodensity contours that fits the data. Because of the lack of a disc in this model, it has much lower minor-axis h_4 coefficients (dashed curve).

The probability of observing a randomly oriented galaxy at inclination angle i is proportional to $\cos i$. On the lower panel of Fig. 6, I plot the maximum a_4/a of the model of NGC 3115 as a function of $\cos i$, showing that for about 40% of all randomly chosen orientations $(a_4/a)_{\text{max}} \lesssim 0.4\%$. Rix & White (1990) have found similar results using razor-thin exponential discs embedded in $R^{-1/4}$ spheroids. As the disc becomes less evident in the photometry, however, its effect on the minor-axis VPs increases (upper panel of figure). Indeed, there is no inclination angle for which the disc would not leave either a photometric or kinematic signature. These results are not confined to NGC 3115: I find similar results using SB’s photometry to model the discy elliptical

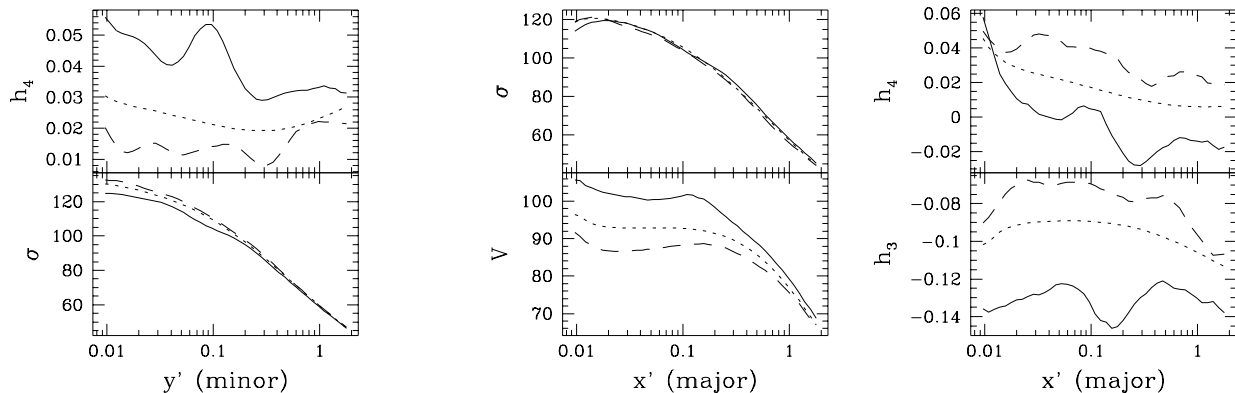


Figure 3. The major- and minor-axis line-of-sight velocity profiles of the models in Fig. 1 (inclination $i = 60^\circ$), obtained by modelling each as a two-integral isotropic rotator. The panel on the left shows the Gauss–Hermite parameters of the minor-axis VPs for the discy (solid curves), boxy (dashed curves) and the original Jaffe (dotted curves) models. The other two panels show the Gauss–Hermite parameters of the major-axis VPs.

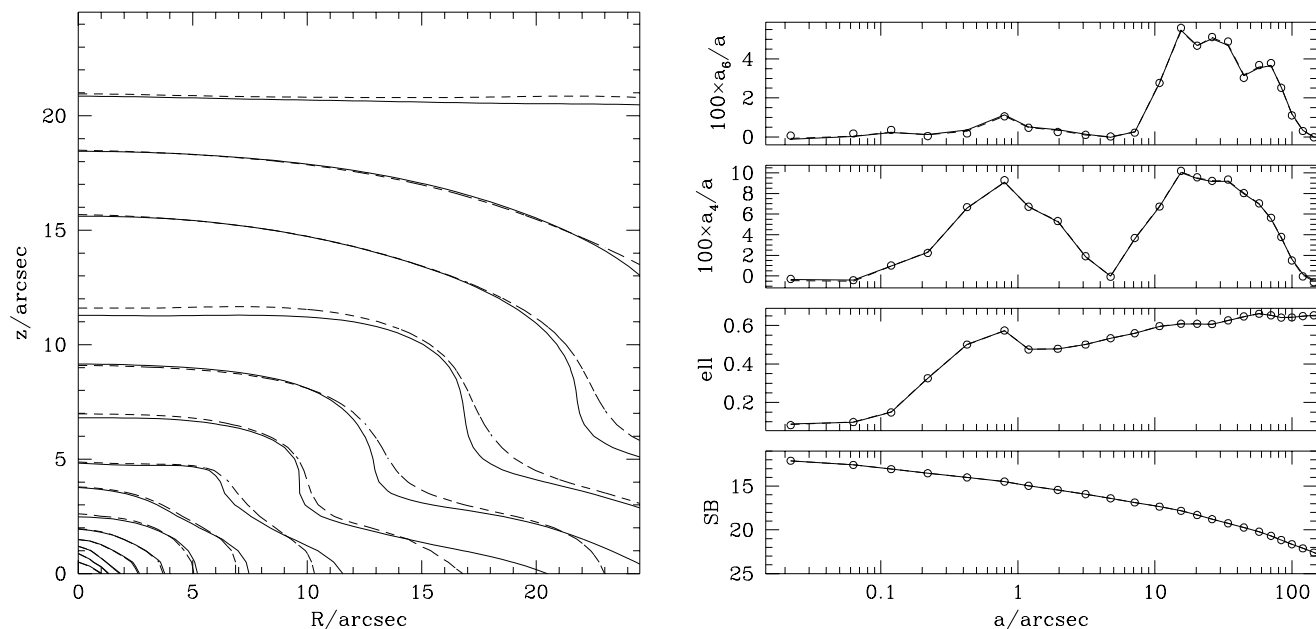


Figure 4. (Left panel) Density distributions $\rho(R, z)$ obtained for NGC 3115 assuming $i = 84^\circ$ (solid contours) and $i = 90^\circ$ (dashed contours). The panel on the right shows that both models project to a reasonable fit to the observed photometry (plotted as the circles).

galaxies NGC 3377 and NGC 4660.

Finally, to understand how the detectability of discs correlates with the disc-to-bulge ratio, I embed discs with a range of luminosities in the toy Jaffe model of the preceding section. Each disc has an exponential radial profile, with unit scale radius and an isothermal $\text{sech}^2(z/2z_0)$ vertical distribution with scale height $z_0 = 0.1$. Fig. 7 shows that for all inclination angles the disc is clearly evident in either the photometry or the kinematics, provided the disc-to-bulge ratio is at least 3%.

5 CONCLUSIONS

It has been known for some time (Rix & White 1990) that it is possible that quite large, almost face-on discs could lurk in elliptical galaxies without leaving any detectable signature in the galaxies' photometry. More sensitive photometry is unlikely to improve the detectability of these discs: Gerhard & Binney (1996) have shown that the deprojection of any axisymmetric galaxy that is not viewed exactly edge-on is formally degenerate to the addition of disc-like konus densities. Using two-integral models of nearby edge-on discy ellipticals, I have shown that hidden discs do, however, leave very strong, easily detectable signatures in the galaxies' minor-

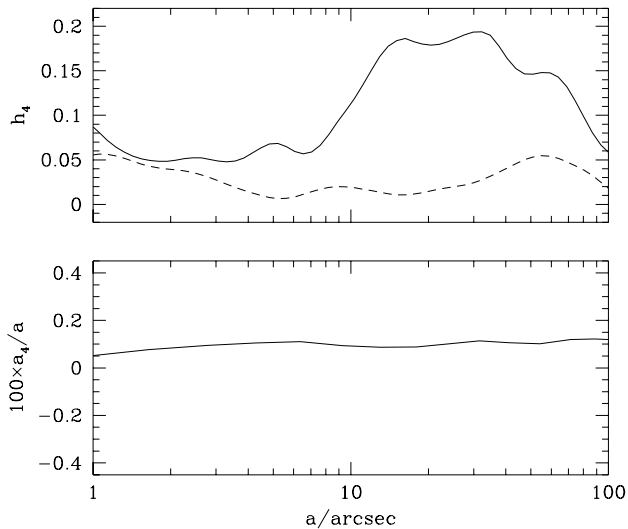


Figure 5. Evidence of the disc in NGC 3115 when viewed almost face-on at $i = 30^\circ$. The small values of the isophotal shape parameters a_4/a on the bottom panel show that there is no photometric sign of the disc at this orientation. On the other hand, the disc leaves a strong signature in the h_4 coefficients of the galaxy’s minor-axis VPs (solid curve in top panel). For comparison, the minor-axis h_4 coefficients of the most closely spheroidal model that fits the $i = 30^\circ$ photometry are plotted as the dashed curve.

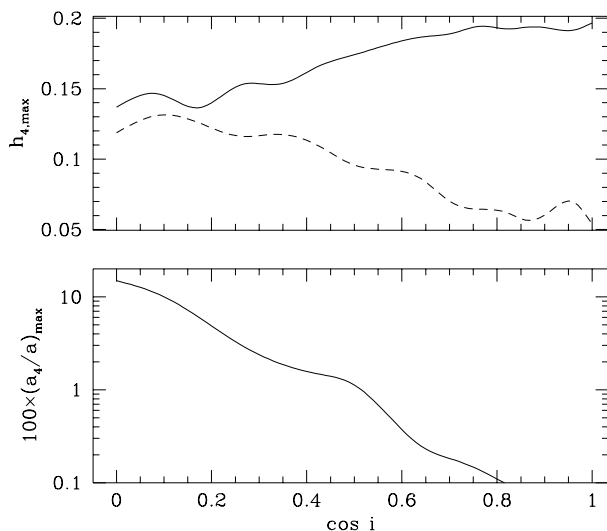


Figure 6. Detectability of the disc in NGC 3115 as a function of inclination angle i . The maximum values of a_4/a for each inclination are plotted on the bottom panel, showing how quickly the disc becomes photometrically invisible with decreasing inclination. The top panel shows the effect that the disc has on the galaxy’s maximum minor-axis h_4 coefficient (solid curve) for each inclination. For comparison, the maximum minor-axis h_4 coefficients of the most closely spheroidal two-integral model that fits the observed photometry are plotted as the dashed curve.

axis VPs, provided the disc-to-bulge ratio is greater than about 3%.

These results are based on two-integral models, but they have important implications for more realistic three-integral

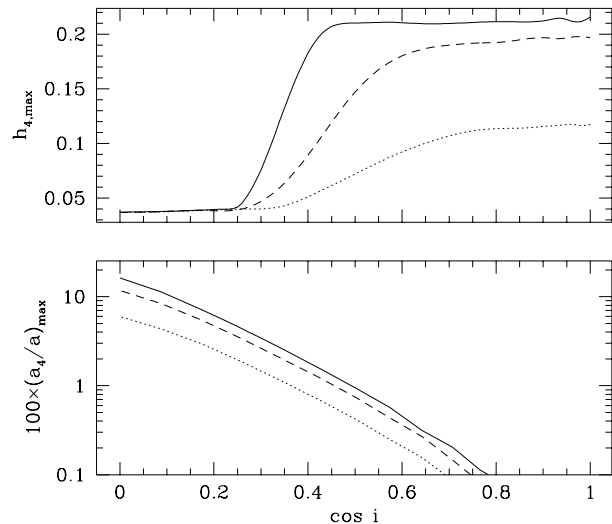


Figure 7. Detectability of the disc in the toy galaxy model described in the text for disc-to-bulge ratios of 0.1 (solid curves), 0.03 (dashed curves) and 0.01 (dotted curves). As in Fig. 6, the bottom panel shows the maximum a_4/a coefficient as a function of inclination, while the top shows the maximum minor-axis h_4 coefficient.

models. The most sophisticated current modelling machinery (e.g., van der Marel et al. 1998; Gebhardt et al. 1998) uses an *assumed* (usually spheroidal) $\rho(R, z)$ and corresponding self-consistent potential to constrain a galaxy’s orbit distribution from its VPs. Given, say, an isotropic galaxy with a weak, invisible face-on disc, it is possible that such machinery could fit the positive h_4 coefficients of the galaxy’s minor-axis VPs using a spheroidal $\rho(R, z)$ with a radially biased orbit distribution. (In principle, a particularly cold disc might leave an unambiguous signature on the VPs, but it is unlikely that this signature would survive the instrumental broadening that real measurements suffer from.) Thus it is important that some attention be focused on modelling galaxies that are known to be close to edge-on (i.e., are discy), so that the uncertainty in the photometric deprojection is minimized.

Ultimately, however, one is interested in all the other galaxies whose inclination angles, density distributions and orbit distributions are unknown. Until more general modelling machinery that “knows” about the orbital structure of edge-on galaxies becomes available, it might be worthwhile relaxing the self-consistency requirement in current models and have them fit to VPs and *photometry*, rather than fitting to an assumed, unobservable $\rho(R, z)$. It would be possible to iterate, using the potentials of the resulting density distributions to generate proper self-consistent models. This could be an informative first step in trying to constrain both the internal shapes and orbital structures of galaxies.

Unfortunately, it is not possible to test these ideas yet because there are currently very few power-law galaxies with high signal-to-noise measurements of minor-axis VPs. Let us hope that this is only a temporary problem.

ACKNOWLEDGMENTS

I thank Ralf Bender, James Binney, David Merritt and the referee, Ortwin Gerhard, for enlightening discussions. Finan-

cial support was provided by NSERC.

REFERENCES

- Bender R., Möllenhoff C., 1987, *A&A*, 177, 71
 Bender R., Surma P., Döbereiner S., Möllenhoff C., Madejsky R., 1989, *A&A*, 217, 35
 Bender R., Saglia R.P., Gerhard O.E., 1994, *MNRAS*, 269, 785
 Binney J., 1985, *MNRAS*, 212, 767
 Faber S.M., et al., 1997, *AJ*, 114, 1771
 Franx M., Illingworth G., de Zeeuw T., 1991, *ApJ*, 383, 112
 Gebhardt K., et al., 1998, submitted to *AJ*
 Gerhard O.E., Binney J., 1996, *MNRAS*, 279, 993
 Jaffe W., 1983, *MNRAS*, 202, 995
 Jedrzejewski R.I., 1987, *MNRAS*, 226, 747
 Kochanek C.S., Rybicki G.B., 1996, *MNRAS*, 280, 1257
 Kormendy J., Bender R., 1996, *ApJL*, 464, 119
 Magorrian S.J., Binney J., 1994, *MNRAS*, 271, 949
 Merritt D., Quinlan G.D., 1998, *ApJ* 498 625
 Metropolis N., Rosenbluth A., Rosenbluth M., Teller A., Teller E., 1953, *J. Chem. Phys.*, 21, 1087
 Press W.H., Flannery B.P., Teukolsky S.A., Vetterling W.T., 1992, *Numerical Recipes in C*, 2nd edn. Cambridge Univ. Press, Cambridge
 Rix H.-W., White S.D.M., 1990, *ApJ*, 362, 52
 Romanowsky A.J., Kochanek C.S., 1997, *MNRAS*, 287, 35
 Rybicki G., 1987, in de Zeeuw T., ed., *Proc. IAU Symp. 127, Structure and dynamics of Elliptical Galaxies*. Reidel, Dordrecht, p. 397
 Scorza C., Bender R., 1995, *A&A*, 293, 20 (SB)
 Statler T., 1994, *ApJ*, 425, 500
 van den Bosch F., 1997, *MNRAS*, 287, 543
 van der Marel R.P., Franx M., 1993, *ApJ*, 407, 525
 van der Marel R.P., Cretton N., de Zeeuw P.T., Rix H.-W., 1998, *ApJ*, 493, 613

APPENDIX A: THE PROJECTION ALONG THE LINE OF SIGHT

The projected surface brightness distribution $\hat{I}(x', y')$ of the density distribution $\rho(R, z)$ is

$$\hat{I}(x', y') = \int_{-\infty}^{\infty} \rho(R, z) dz' \quad (11)$$

where (R, z) is related to (x', y', z') through the rotation

$$\begin{pmatrix} x \\ y \\ z \end{pmatrix} = \begin{pmatrix} 1 & 0 & 0 \\ 0 & \cos i & \sin i \\ 0 & \sin i & -\cos i \end{pmatrix} \begin{pmatrix} x' \\ y' \\ z' \end{pmatrix}, \quad (12)$$

and $R^2 = x^2 + y^2$. With the substitution

$$z' = (x'^2 + y'^2)^{1/2} \sinh u, \quad (13)$$

the integral in equation (11) can be approximated using the trapezium rule as

$$\hat{I}(x', y') \simeq (x'^2 + y'^2)^{1/2} du \sum_{k=0}^n \rho(R_k, z_k) \cosh u_k, \quad (14)$$

with u_0 and u_n chosen such that the corresponding z' lie just outside the edges of the model density grid, and the intermediate u_k spaced linearly between them with $du \equiv (u_n - u_0)/n$. The points R_k and z_k are the intrinsic coordinates of the point (x', y', z'_k) in the k^{th} term in the sum. To ensure fair sampling of the grid points along the line of

sight, I choose $n = 4n_a$.

Since $\rho(m, \theta)$ is obtained by linear interpolation in $\mathcal{R}(m, \theta) \equiv \log \rho(a, \theta)$ this sum can be rewritten in the form

$$\sum_{k=0}^n E_k \exp \left(A_k \mathcal{R}_{a_k, b_k} + B_k \mathcal{R}_{a_{k+1}, b_k} + C_k \mathcal{R}_{a_k, b_{k+1}} + D_k \mathcal{R}_{a_{k+1}, b_{k+1}} \right), \quad (15)$$

where the (x', y') -dependent coefficients $A_k \dots E_k$, a_k and b_k do not depend on \mathcal{R} and so only have to be evaluated once for each (x'_{ij}, y'_{ij}) . Expressions for these constants are quite easy to work out, but tedious to write out.

If, like Romanowsky & Kochanek (1997), I had chosen to interpolate linearly in ρ rather than $\log \rho$, then equation (15) would be replaced by an even simpler expression. However, this interpolation-in- ρ scheme is unable to represent steeply cusped density distributions accurately: using it, the RMS error in the numerical projection of the toy model used in Section 3 is 1.6%, rather than the 0.05% obtained with interpolation in $\log \rho$. On doubling n_m to increase the resolution of the radial m_i grid, the error goes down only slightly to 1.3%. (On the other hand, the error in the $\log \rho$ scheme goes down to 0.015%.) Thus, the extra expense that interpolating in $\log \rho$ brings to the numerical projection equation (15) is easily justifiable.

This paper has been produced using the Royal Astronomical Society/Blackwell Science \TeX macros.